ARMY RESEARCH LABORATORY

Biaxial Testing of Composites - A Study of The Disk Specimen

Paul Cavallaro, Lisa Gee, and
Nikos Tsangarakis

ARL-TR-690

April 1995

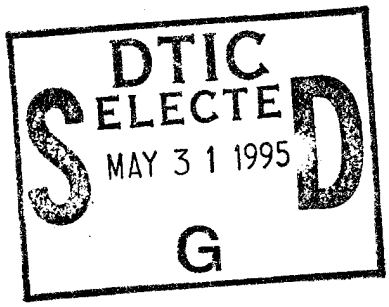

19950530 021

Approved for public release; distribution unlimited.

The findings in this report are not to be construed as an official Department of the Army position unless so designated by other authorized documents.

Citation of manufacturer's or trade names does not constitute an official endorsement or approval of the use thereof.

Destroy this report when it is no longer needed. Do not return it to the originator.

REPORT DOCUMENTATION PAGE

Form Approved
OMB No. 0704-0188

1. AGENCY USE ONLY *(Leave blank)*	2. REPORT DATE	3. REPORT TYPE AND DATES COVERED
	April 1995	Final 1993-1994

4. TITLE AND SUBTITLE

Biaxial Testing of Composites - A Study of the Disk Specimen

5. FUNDING NUMBERS

6. AUTHOR(S)

Paul Cavallaro, Lisa Gee, and Nikos Tsangarakis

7. PERFORMING ORGANIZATION NAME(S) AND ADDRESS(ES)

Army Research Laboratory
Watertown, MA 02172-0001
ATTN: AMSRL-MA-PC

8. PERFORMING ORGANIZATION REPORT NUMBER

ARL-TR-690

9. SPONSORING/MONITORING AGENCY NAME(S) AND ADDRESS(ES)

10. SPONSORING/MONITORING AGENCY REPORT NUMBER

11. SUPPLEMENTARY NOTES

12a. DISTRIBUTION/AVAILABILITY STATEMENT

Approved for public release; distribution unlimited.

12b. DISTRIBUTION CODE

13. ABSTRACT *(Maximum 200 words)*

The strain fields in composite disks loaded with a pin on one side while the other side was simply supported circumferentially, were examined. Finite Element Analysis (FEA) results indicated that in a balanced, $[(0_2/90_2)_2]_S$ cross-ply composite, the in-plane principal strains were nearly equal and constant within the load pin radius. For a $[(0/90)_S/(90/0)_S]_S$ balanced laminate, FEA results indicated an equi-biaxial principal strain field within the same radius. The interlaminar shear strains were shown to be constant through the disk thickness and depended greatly on the interfiber distance and fiber diameter. It was shown that large, closely spaced fibers could intensify the shear strain field to the extent of forming single or multiple delaminations.

14. SUBJECT TERMS

Composites, Biaxial Loading, Interlaminar Shear, Finite Element Analysis

15. NUMBER OF PAGES

32

16. PRICE CODE

17. SECURITY CLASSIFICATION OF REPORT	18. SECURITY CLASSIFICATION OF THIS PAGE	19. SECURITY CLASSIFICATION OF ABSTRACT	20. LIMITATION OF ABSTRACT
Unclassified	Unclassified	Unclassified	UL

SYMBOLS

b	Load Pin Radius
E_{LF}	Effective Longitudinal Flexure Modulus of Laminate
E_{TF}	Effective Transverse Flexure Modulus of Laminate
h	Thickness of Matrix Material
K_{LS}	Local Shear Strain Concentration Factor
R	Fiber Radius
R_{LP}	Load Pin Radius
t	Disk Thickness
U	Displacement along Global X-Axis
U'	Rotation along Global X-Axis
V	Displacement along Global Y-Axis
V'	Rotation along Global Y-Axis
V_f	Fiber Volume Fraction
W	Displacement along Global Z-Axis
W'	Rotation along Global Z-Axis
{X,Y,Z}	Global Coordinate System
{1,2}	Principal Lamina (Material) Coordinate System
ε_{11}	Extensional Strain along Principal 1-Axis
ε_{22}	Extensional Strain along Principal 2-Axis
ε_{12}	Shear Strain in {1,2} Plane
γ_{xz}	Interlaminar Shear Strain

TABLE OF CONTENTS

	PAGE
INTRODUCTION	1
FINITE ELEMENT MODELING	2
MODELING THE EFFECT OF FIBER SIZE AND SPACING	7
DISCUSSION	10
CONCLUSIONS AND RECOMMENDATIONS	12
REFERENCES	14-15
APPENDIX	
TABLES	16
FIGURES	17-28

INTRODUCTION

The need to reduce weight of structures has led to the development of numerous fiber reinforced composite materials. Due to the lack of a well established database, these new materials can not be utilized to their full potential. The majority of available mechanical property data in the open literature was generated under uniaxial loading which represents a small fraction of existing structural loading schemes. Attempts to generate composite property data under biaxial loading have been made by several investigators using various specimen types. A review of the multiaxial loading tests for composite materials is provided by Chen and Matthews[1]. A brief criticism of the drawbacks of these specimens was presented in an earlier article[2]. A new specimen for the determination of the mechanical properties of composites under biaxial flexure loading was introduced in the latter publications. Disk specimens were used to generate biaxial property data for both cross-ply[2] and unidirectional[3] aluminum matrix composites and a graphite fiber/epoxy cross-ply composite[4]. The main advantages of the disk specimen were: (1) minimal machining, (2) small volume (5 cm diameter for thicknesses up to 3 mm), (3) no special grips or loading fixtures required and (4) near constant strain contours within the loading area.

The disk specimen was used by several investigators to conduct biaxial flexure tests of isotropic ceramic materials. These investigations included analyses of the disk specimen by Finite Element Methods (FEM). Three variations of the biaxial flexure test exist for homogeneous isotropic materials[5]:

a. Ball-on-Ring Test

b. Piston-on-Three-Ball Test

c. Ring-on-Ring Test

The piston-on-three-ball test is the ASTM ANSI/F394-78 standard (1978, part 43). Recently, Shetty et al[6] and Chao et al[7] introduced the hydraulic-pressure-loading test which loads the disk uniformly.

The present work evaluates the biaxial strain field of the disk for continuous fiber reinforced composite materials with both finite element and closed form analytical methods. Effects of the disk geometry and the material characteristics on the resulting strain fields were explored, modeled and discussed. Another intent of this work was to further promote the adoption of the disk and related test procedures as a standard biaxial flexure specimen.

FINITE ELEMENT MODELING

The material considered for the finite element analysis was a 16-ply graphite/epoxy composite with a balanced cross-ply sequence of $[(0_2/90_2)_2]_S$. Material properties corresponded to Hercules (TM) 3501-6 epoxy resin/AS-4 continuous graphite fiber prepreg. Resin and lamina properties are provided in Tables (1) and (2), respectively. The processed laminate had a 60% fiber volume. Diameter and thickness values of the disk were 50.8mm and 2.25mm, respectively.

The loading arrangement for this analysis is shown in Fig. (1). Shetty et al[5] found that when ceramic disks deflect biaxially under pin loading, the

concentric loading converted from initially uniform to ring-type. Ritter et al[8] made the same conclusion. Ring-type loading was confirmed by the appearance of ring-shaped markings under the loading pin on the compressive surfaces of tested disks[2-4]. Thus, all strain profiles discussed herein corresponded to concentric ring-type loading.

Modeling of the 16-ply laminated disk was accomplished using the NISA-II[9](TM) finite element analysis program. The Reissner-Mindlin approach[10] revealed the problem of shear locking which is associated with bending of thin plates. Papadopoulos and Taylor[11] described a triangular element with a unique interpolational approach that avoids shear locking. The shear locking problem was overcome in the current model through the use of higher-ordered element formulations. A combination of NISA type 32, 3-D laminated composite, quadrilateral and triangular general shell elements were used. The formulations used quadratic (6-noded triangles and 8-noded quadrilaterals) rather than linear interpolation functions and included transverse shear deformation capability. A ring of triangular elements was necessary to model the center of the disk due to the converging shape of the quadrilateral elements in this vicinity. The analysis performed was linearly elastic and incorporated several assumptions from Classical Laminated Plate Theory[12] (CLPT), namely: (1) the laminate consisted of multiple layers of perfectly bonded orthotropic materials, (2) no through-thickness normal deformations were allowed, and (3) the bond layers between plies were infinitesimally thin. A further assumption resulting from the NISA-II element formulation was that shell elements possessed infinite rotational stiffness about the normal direction to their surface.

The disk specimen possessed quarter symmetry in terms of material properties, boundary, and loading conditions collectively. Therefore, one quadrant was discretized using 330 elements and 1057 nodal points. Global axes (X,Y) were taken parallel to the 0° and 90° ply directions, respectively. The principal (or material) axes (1,2) for each ply were aligned so that the 1-axis was parallel to the fiber direction and the 2-axis was perpendicular to the fiber direction. The displacement boundary conditions are shown in Fig. (2). In this figure, U, V, and W represent the displacements along the X, Y, and Z axes, respectively and U', V', and W' represent rotations along the same axes. Quarter symmetry was enforced by restraining the following Degrees of Freedom (DOF):

DOF		LOCATION
V=U'=0	at	X=X, Y=0, Z=0
U=V'=0	at	X=0, Y=Y, Z=0
U=V=U'=V'=0	at	X=0, Y=0, Z=0

The outer edge of the disk was restrained from displacement in the Z-direction by setting W=0 at nodes along this edge. A distributed load of 4.45kN was applied as a series of concentrated forces at nodal points defining a circle of radius "b". Radius "b" was equal to the load pin radius (6.1mm) used in tests by Tsangarakis et al[2-4]. In further accordance with CLPT[12], the in-plane strains were assumed linearly dependent with the distance from the neutral plane. The neutral plane was assumed to be coincident with the mid-plane of the disk according to CLPT for symmetric laminates.

The deflected disk shape, superimposed with the unloaded configuration, and the transverse (out-of-plane) displacement contours are shown in Figs. (3) and

(4), respectively. Note the asymmetrical profile of the transverse displacement contours in Fig.(4) which resulted directly from the anisotropy of the laminate. Figure (5) shows in-plane stress contours for the compressive surface layer. The compressive surface layer alone was examined since stress and strain fields of the remaining layers varied linearly with the distance from the laminate neutral plane. Stress output was automatically extrapolated from the Gauss (integration) points to the nodes, while strains were obtained at element centroids. In-plane strain versus radial distance plots of Figs. (6-8) show principal and shear strains plotted against rays of element centroidal locations. Ray angles were measured from the global X-axis. Results indicated that principal strains ε_{11} = -0.0137 m/m and ε_{22} = -0.0155 m/m and formed a nearly equi-biaxial strain field within the load pin radius. At the center of the disk, the two principal strains varied by 12%. The in-plane shear strain at any orientation within the load pin radius converged to zero. Localized effects of the strain field due to the applied loading appeared as knees on each strain component curve and decayed towards the center approaching constant values. Furthermore, the principal strains became invariant to angular position for points approaching the center. Finite element modeling by Ritter et al[8] and experimental tests by Shetty et al[5] confirmed the existence of similar localized stress magnifications at the load point for isotropic ceramic disks. Outside of the load pin radius, the principal and shear strains had significant dependence upon angular position. These strain profiles were in agreement with strain gage measurements made Tsangarakis et al[2-4]. The peak out-of-plane deflection for a load of 4.45kN was 2.835×10^{-3} m occurring at the center of the disk.

A special case of interest was investigated in which a symmetric cross-ply laminate stacking sequence was optimized to provide an equi-biaxial strain field within the load pin radius. In particular, the stacking sequence resulting in equivalent laminate flexure moduli E_{LF} and E_{TF} (where E_{LF} designated the longitudinal or X-direction flexure modulus and E_{TF} designated the transverse or Y-direction flexure modulus) was determined. For symmetric laminates, the following compliance equations by Tsai[13] were used to determine the flexure moduli E_{LF} and E_{TF}:

$$E_{LF} = 1/d_{11}^{*} \quad \text{and} \quad E_{TF} = 1/d_{22}^{*}$$

where:

$$[d^{*}] = [d]h^{3}/12 = \text{Normalized Bending Compliance}$$

and:

$$h = \text{Laminate Thickness}$$

$$[d] = [D]^{-1} = \text{Laminate Bending Compliance Matrix}$$

$$[D] = \text{Laminate Bending Stiffness Matrix}$$

Figure (9) shows the variations in flexure moduli E_{LF} and E_{TF} for 4 different symmetric cross-ply laminates. The $[(0/90)_S/(90/0)_S]_S$ laminate yielded equivalent values of E_{LF} and E_{TF} at 63.30 GPa. The previous FEA model was updated to include the optimized ply stacking sequence and re-executed. Compressive surface principal strains ε_{11} and ε_{22} were equal to -0.0143 m/m within the load pin radius and became invariant to angular position for points approaching the disk center. Peak out-of-plane deflection was 2.805×10^{-3} m occurring at the center of the disk.

MODELING THE EFFECT OF FIBER SIZE AND SPACING

Considering a 0° ply, the two neighboring fibers shown in Fig.(10) have radius R and are separated by matrix material of thickness h. The coordinate system of this figure is the same as that used in the finite element model (see Fig. 2). Let the fibers be designated as i and i+1 and experience the strains $\varepsilon_{xx}(x,y,z_i)$ and $\varepsilon_{xx}(x,y,z_{i+1})$, respectively. Further assume that the:

1. Fibers are well bonded to the matrix.
2. Fibers and matrix obey Hooke's Law.
3. Deformation "w" along the z-axis is negligible compared to deformations "u" and "v" along axes x and y, respectively.
4. Principal strains on the tensile side of the disk are equal and constant on a given plane and within the load pin region.
5. Fibers are subjected to only uniform axial loads.

The interlaminar shear strain γ_{zx} experienced by the matrix will be:

$$\gamma_{zx} = dw/dx + du/dz \qquad (1)$$

From the third assumption, the displacement w and its derivative along the z-axis are negligible. Thus, the first term in the right side of Eq.(1) may be omitted. Using the model discussed by Puppo and Evensen[14], Garg et al[15], and recently by Gao and Reifsnider[16] for a balanced laminated composite, the interlaminar shear strain can be approximated as:

$$\gamma_{zx} = du/dz = (u_{i+1}-u_i)/h \qquad (2)$$

Let z_i be the distance of fiber i from the mid-plane. If t is the disk thickness and $\varepsilon_{xx(t/2)}$ is the principal strain of the outermost fiber (z=t/2), then:

$$\varepsilon_{xx}(x,y,z_i) = (2z_i/t)\ \varepsilon_{xx(t/2)} \tag{3}$$

The strain $\varepsilon_{xx}(x,y,z_i)$ may also be expressed as:

$$\varepsilon_{xx}(x,y,z_i) = du_i/dx \tag{4}$$

Integrating Eq.(4):

$$u_i = \int_o^x \varepsilon_{xx}(x,y,z_i)dx \tag{5}$$

Substituting the principal strain from Eq.(3) into Eq.(5):

$$u_i = \int_o^x \varepsilon_{xx(t/2)}(2z_i/t)dx \tag{6}$$

And because $\varepsilon_{xx(t/2)}$ is constant per assumption 4:

$$u_i = \varepsilon_{xx(t/2)}(2z_i/t)x \tag{7a}$$

$$u_{i+1} = \varepsilon_{xx(t/2)}(2z_{i+1}/t)x \tag{7b}$$

Substituting Eqs.(7a,b) into Eq.(2):

$$\gamma_{zx} = 2h\varepsilon_{xx(t/2)}[z_{i+1}-z_i]x/t \tag{8}$$

From Fig.(10), the difference $(z_{i+1} - z_i)$ may be expressed as (2R + h). Substituting into Eq.(8):

$$\gamma_{zx} = 2\varepsilon_{xx(t/2)}[1+(2R/h)]x/t \tag{9}$$

The same consideration is followed for shear strain γ_{zy} in a 90° layer where the x subscripts and coordinate term are replaced by y. This treatment, of course, is valid for balanced composites.

The shear strains γ_{zx} and γ_{zy} in 90° and 0° layers, respectively, are found through the usual treatment with the theory of bending of thin composite plates[15]. These strains are maximized at locations designated as points A in Fig.(11), that is, where the matrix thickness h is minimal. At remote locations designated as points B, the shear strain is minimal.

Equation (9) indicates that the interlaminar shear strain depends on the disk thickness, fiber radius, and interfiber matrix thickness. The interlaminar shear strain also depends on distance x and the strain $\varepsilon_{xx(t/2)}$. For failure to occur by matrix shearing, the interlaminar shear strain must exceed a critical value γ^*. This is the value of the shear strain required to form a delamination. From Eq.(9), it is evident that as the ratio 2R/h increases, the matrix shear strain increases. Note that this shear strain is independent of the distance from the fibers to the neutral plane. Larger fibers will favor the formation of delaminations. When fibers are bent or misaligned, the matrix layer thickness h may decrease between two neighboring fibers leading to delamination. Thus the ratio 2R/h may be considered as a local shear strain concentration factor, K_{LS}. Because this ratio may vary at many locations within the disk, formation of multiple delaminations is possible.[4]

DISCUSSION

The strain profiles depicted in Figs.(6,7) were verified by Finite Element Analysis and experimentally with strain gages[2,4] for a balanced, cross-ply $[(0_2/90_2)_2]_S$ fiber reinforced composite. The two principal strains ε_{11} and ε_{22} were found to vary within 12% and were constant within the load pin region. These observations were also found for isotropic ceramic disks by Ritter et al[8]. The two principal strains were zero at the disk mid-thickness[2]. The ability to tailor fiber reinforced composite laminates resulted in an optimized ply stacking sequence, namely $[(0/90)_S/(90/0)_S]_S$, which yielded an equi-biaxial principal strain field within the load pin radius.

In the unidirectional aluminum composite disk[3], the maximum principal tensile strain (parallel to the fibers) was constant within the load pin area as observed by strain gage measurements. The principal tensile strain perpendicular to the fibers was maximal at the disk center and decayed to zero thereafter towards the disk edge.

As Eq.(9) indicates, within the load pin region, the interlaminar shear strain increases with distance from the center of the disk. Letting x = b, where b is the load pin radius, the interlaminar shear strain at the edge of the load pin is:

$$\gamma_{zx} = \varepsilon_{xx(t/2)}(1 + 2R/h)2b/t \qquad (10)$$

The interlaminar shear strain is maximized at the disk edge and is approximated as:

$$\gamma_{zx} = 2\varepsilon_{xx(t/2)}(1 + 2R/h)(r-b)/t \qquad (11)$$

Since the interlaminar shear strain is dependent upon the ratio 2R/h, large or closely spaced fibers will induce higher shear strain values. Similar conclusions were drawn by Ramsteiner and Theysohn[17] for a short glass fiber reinforced organic composite. These investigators found that as the fiber radius increased, the failure tensile strength decreased. Thus, evidence exists that larger fibers entail higher local shear strain concentrations (K_{LS}). The ratio 2R/h depends on the fiber volume fraction, V_f, of the composite. A simple geometrical consideration shows that the ratio dependence on V is:

$$2R/h = 2/(\sqrt{\pi/V_f} - 2) \qquad (12)$$

The above equation indicates that as the fiber volume fraction increases, so does the aspect ratio 2R/h. For fiber volume fractions of 0.1 and 0.6, the respective values of the aspect ratio are 0.555 and 6.940. These values represent the lower and upper bounds, respectively, of the local shear strain concentration factor K_{LS} which is plotted in Fig.(12).

It was shown that the interlaminar shear strain is independent of the distance from the disk mid-plane. When the value of the interlaminar shear strain, as given by Eq.(9), exceeds a critical value, a matrix crack may form by shear. Because K_{LS} may vary greatly (0.55 to 6.940) due to uneven distribution of the fibers, the matrix shear strength may be exceeded at many locations simultaneously. Thus, multiple cracks may form at different locations. Such cracks are shown in Fig.(13) for a silicon carbide fiber

(0.14mm diameter) reinforced aluminum composite[2], and in Fig.(14) for a carbon fiber reinforced resin composite[4]. In Fig.(15), a C-scan of a failed organic composite disk shows the multiplicity of the generated matrix cracks. Existing theories as those of mixed modes fracture energy, shear lag, and the empirical mixed mode fracture toughness of Wang et al[18] do not explain the formation of multiple delaminations.

An estimate of the interlaminar shear strength of the organic composite[4] was obtained by testing two sets of short beam shear specimens in accordance with the ASTM D2344 procedure. The specimen size was 1.9mm x 6.3mm x 25mm. Each set consisted of six coupons. The estimates of the interlaminar shear strength were 44.5 $\pm$ 9.5 MPa and 38.7 $\pm$ 7.5 MPa for the first and second set, respectively. The average was 41.6 MPa which represented a gross estimate of the interlaminar shear strength of the composite.

CONCLUSIONS AND RECOMMENDATIONS

The strain fields in fiber reinforced laminated composite disks loaded with a pin on one side, while the other side was simply supported cicumferentially, were examined. Finite element analysis results indicated that in a balanced, $[(0_2/90_2)_2]_S$ cross-ply composite, the in-plane principal strains were nearly equal and constant within the load pin radius. An optimized cross-ply stacking sequence of $[(0/90)_S/(90/0)_S]_S$ resulted in an equi-biaxial principal strain field within the load pin radius. The interlaminar shear strains were shown to be constant through the disk thickness and greatly dependent upon interfiber distance and fiber diameter. It was shown that large, closely spaced fibers could intensify the shear strain field to the extent of forming

single or multiple delaminations. Because perfect fiber alignment can not be achieved throughout the laminate thickness, the present test method can not be used to determine the interlaminar shear strength of fiber reinforced composites. However, the disk specimen would be useful in comparative studies as a quality control tool and to assess the response of the composite to biaxial flexure loading.

REFERENCES

1. Chen, A.S. and Matthews, F.L., "A Review of Multiaxial/Biaxial Loading Tests for Composite Materials", Composites, vol. 24, No. 5, July 1993, pp. 395-406.

2. Tsangarakis, N. and Pepi, M., "Biaxial Flexing of a Fiber Reinforced Aluminum Composite", Journal of Composite Materials, vol. 24, No. 7, July 1990, pp. 770-785.

3. Tsangarakis, N. and Pepi, M., "Biaxial Flexing of a Unidirectionally Reinforced Aluminum Composite", Journal of Composite Materials, vol. 26, No. 14, 1992, pp. 2060-2075.

4. Tsangarakis, N. and Taleghani, B., "Biaxial Flexural Testing of a Carbon Fiber Reinforced Epoxy Composite", Submitted for publication by Journal of Composite Materials, 1995.

5. Shetty, D.K., Rosenfield, A.R., McGuire, P., Bansal, G.K., and Duckworth, W.H., "Biaxial Flexure Tests for Ceramics", Ceramics Bulletin, vol. 59, No. 12, 1980, pp. 1193-1197.

6. Shetty, D.K., Rosenfield, A.R., Duckworth, W.H., Held, P.R., "A Biaxial-Flexure Test for Evaluating Ceramics Strengths", American Ceramics Society Journal, vol. 66, No. 1, January 1983, pp. 36-42.

7. Chao, L.Y., Shetty, D.K., "Reliability Analysis of Structural Ceramics Subjected to Biaxial Flexure", American Ceramics Society Journal, vol. 74, No. 2, February 1991, pp. 333-344.

8. Ritter, J.E. Jr., Jakus, K., Batakis, A., Bandyopadhyay, N., "Appraisal of Biaxial Testing", Journal of Non-Crystalline Solids, No.s 38 and 39, 1980, pp. 419-424.

9. NISA-II, Version 92.0, Engineering Mechanics Research Corporation, Troy Michigan.

10. Mindlin, R.D., "Influence of Rotary Inertia and Shear on Flexural Motions of Isotropic Elastic Plates", Journal of Applied Mechanics, vol. 18, No. 1, March 1951, pp. 31-38.

11. Papadopoulos, P. and Taylor, R.L., "A Triangular Element Based on Reissner-Mindlin Plate Theory", International Journal of Numerical Methods in Engineering, vol. 30, No. 5, 1990, pp. 1029-1050.

12. Jones, R.M., "Mechanics of Composite Materials", 1975, Hemisphere Publishing Co., pp. 147-152.

13. Tsai, S.W., "Composites Design - 1986", 1986, Think Composites, Section 8, pp. 8.1-8.3.

14. Puppo, A.H. and Evensen, H.A., "Interlaminar Shear in Laminated Composites under Generalized Plane Stress", Journal of Composite Materials, vol. 4, April 1970, pp. 204-220.

15. Garg, S.K., Svalbonas, V., and Gurtman, G.A., "Analysis of Structural Composite Materials", Ch. 10, pp. 279-280, Marcel Dekker, Inc., New York, 1973.

16. Gao, Z., and Reifsnider, K.L., "Micromechanics of Tensile Strength in Composites Systems", ASTM STP 1156, 1993, pp. 453-470.

17. Ramsteiner, F., and Theysohn, R., "The Influence of Fibre Diameter on the Tensile Behavior of Short Glass Fibre-Reinforced Polymers", Composites Science and Technology, vol. 24, No. 3, 1985, pp. 231-240.

18. Wang, S.S., Chim, E.S. and Socie, D.F., "Biaxial Fatigue of Fibre-Reinforced Composite at Cryogenic Temperature, Part 1: Fatigue Fracture Life and Mechanisms", Journal of Engineering Material Technology, No. 104, 1982, pp. 128-136.

APPENDIX

TABLE 1 - PROPERTIES OF THE 3501-6 RESIN

Ultimate Tensile Strength, UTS = 70 MPa

Elastic Modulus, E = 4.4 GPa

Tensile Strain-to-Failure, ε_f = 0.017 m/m

TABLE 2 - UNIDIRECTIONAL PROPERTIES OF 3501-6 EP/60% AS-4 CARBON FIBER PREPREG

Elastic Modulus, E_{11} = 115 GPa [15]

Elastic Modulus, E_{22} = 11 GPa [15]

Major Poisson's Ratios, $\nu_{12} = \nu_{13}$ = 0.27 [16]

Minor Poisson's Ratios, $\nu_{21} = \nu_{31}$ = 0.02 [16]

Ultimate Longitudinal Tensile Strain, ε_{11} = 0.0156 m/m [16]

Ultimate In-Plane Shear Strain, ε_{12} = 0.0057 m/m [16]

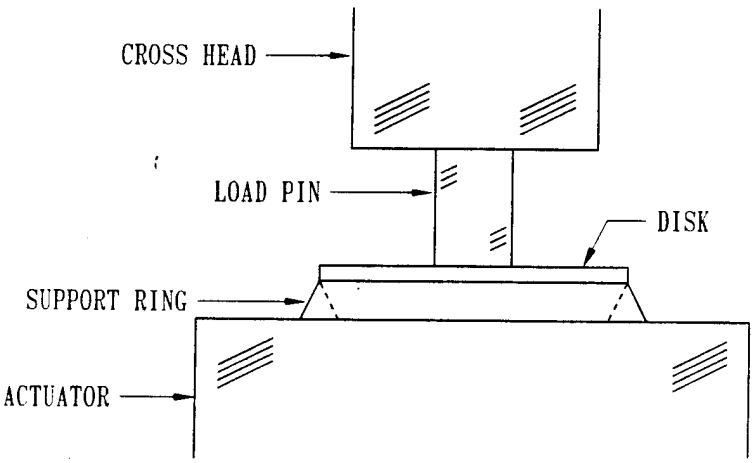

Fig.(1) LOADING ARRANGEMENT OF BIAXIAL DISK SPECIMEN

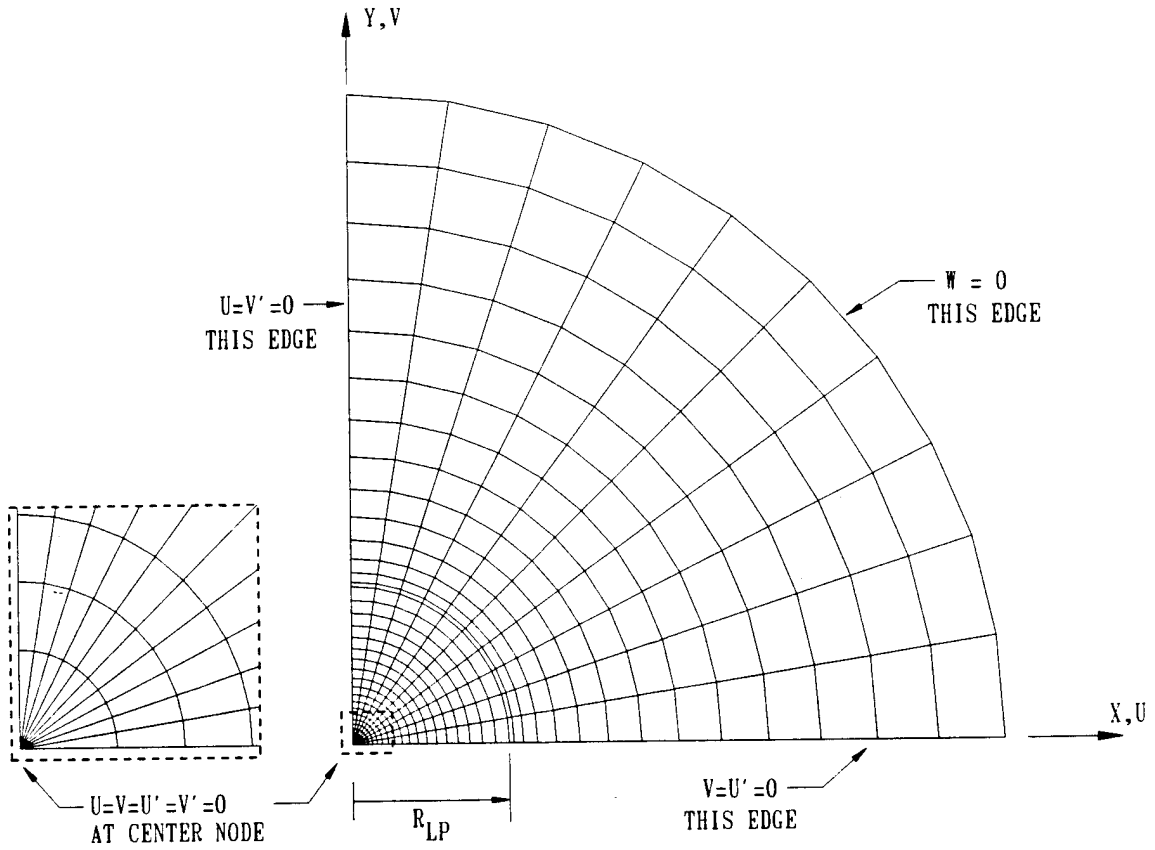

Fig.(2) DISK FINITE ELEMENT QUARTER SYMMETRY MODEL

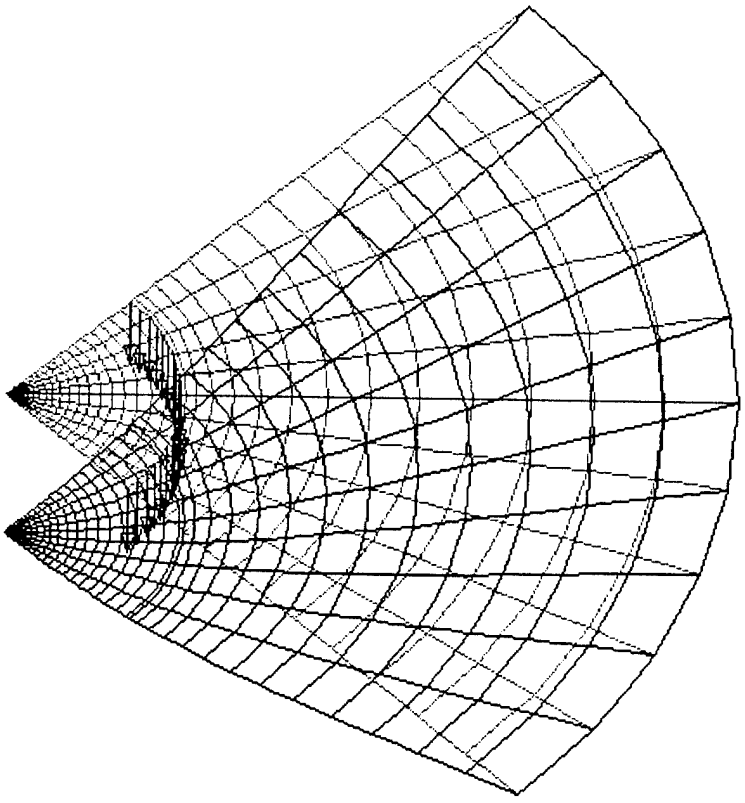

Fig.(3) DEFORMED AND UNLOADED DISK GEOMETRIES

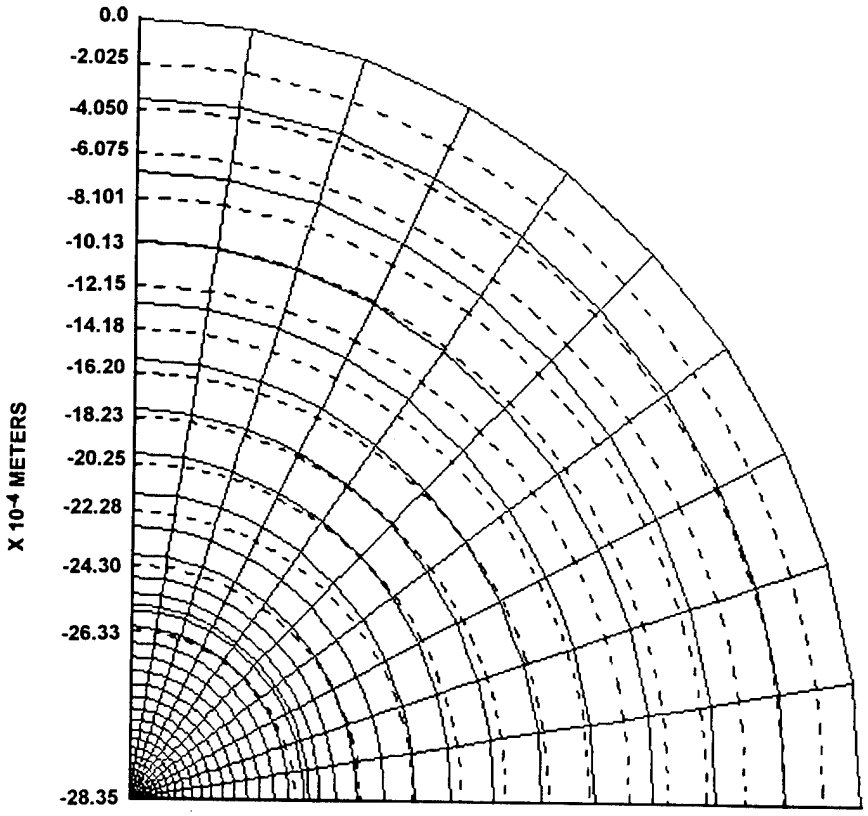

Fig.(4) TRANSVERSE DISPLACEMENTS OF DISK MID-PLANE

σ_{11} x 10^7 GPa

MAX	2.186
13	-10.11
12	-22.41
11	-34.71
10	-47.01
9	-59.31
8	-71.61
7	-83.91
6	-96.21
5	-108.5
4	-120.8
3	-133.1
2	-145.4
1	-157.7
MIN	-170.0

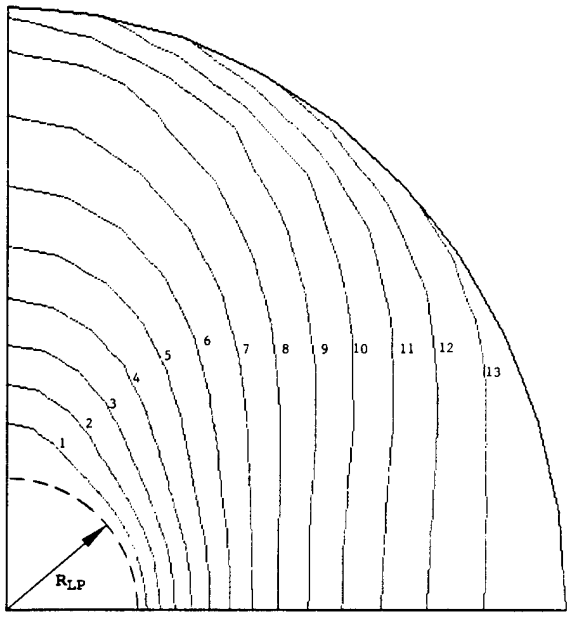

σ_{22} x 10^6 GPa

MAX	-5.649
13	-21.30
12	-36.94
11	-52.59
10	-68.24
9	-83.88
8	-99.53
7	-115.2
6	-130.8
5	-146.5
4	-162.1
3	-177.8
2	-193.4
1	-209.1
MIN	-224.7

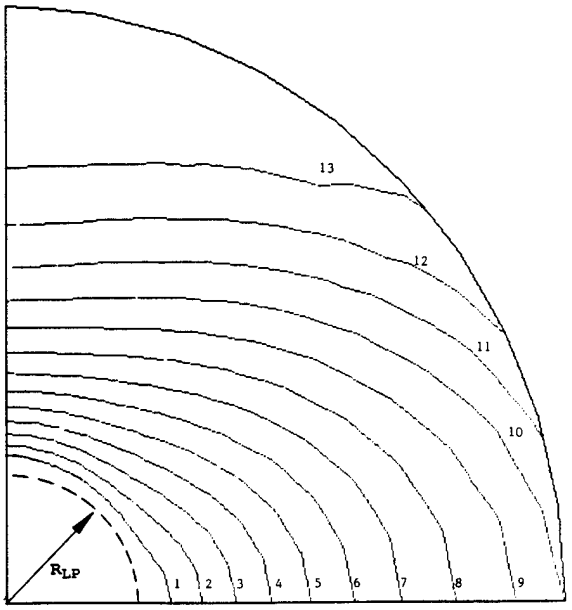

σ_{12} x 10^5 GPa

MAX	719.2
13	663.5
12	607.8
11	552.0
10	496.3
9	440.6
8	384.9
7	329.2
6	273.5
5	217.7
4	162.0
3	106.3
2	50.59
1	-5.130
MIN	-60.85

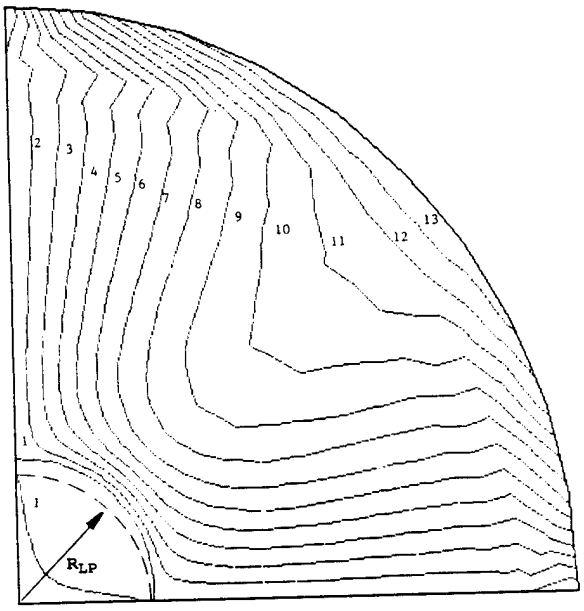

$[(0_2/90_2)_2]_S$

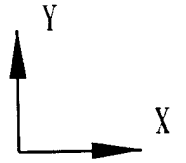

Fig.(5) PRINCIPAL STRESSES σ_{11}, σ_{22}, σ_{12} - COMPRESSIVE SURFACE

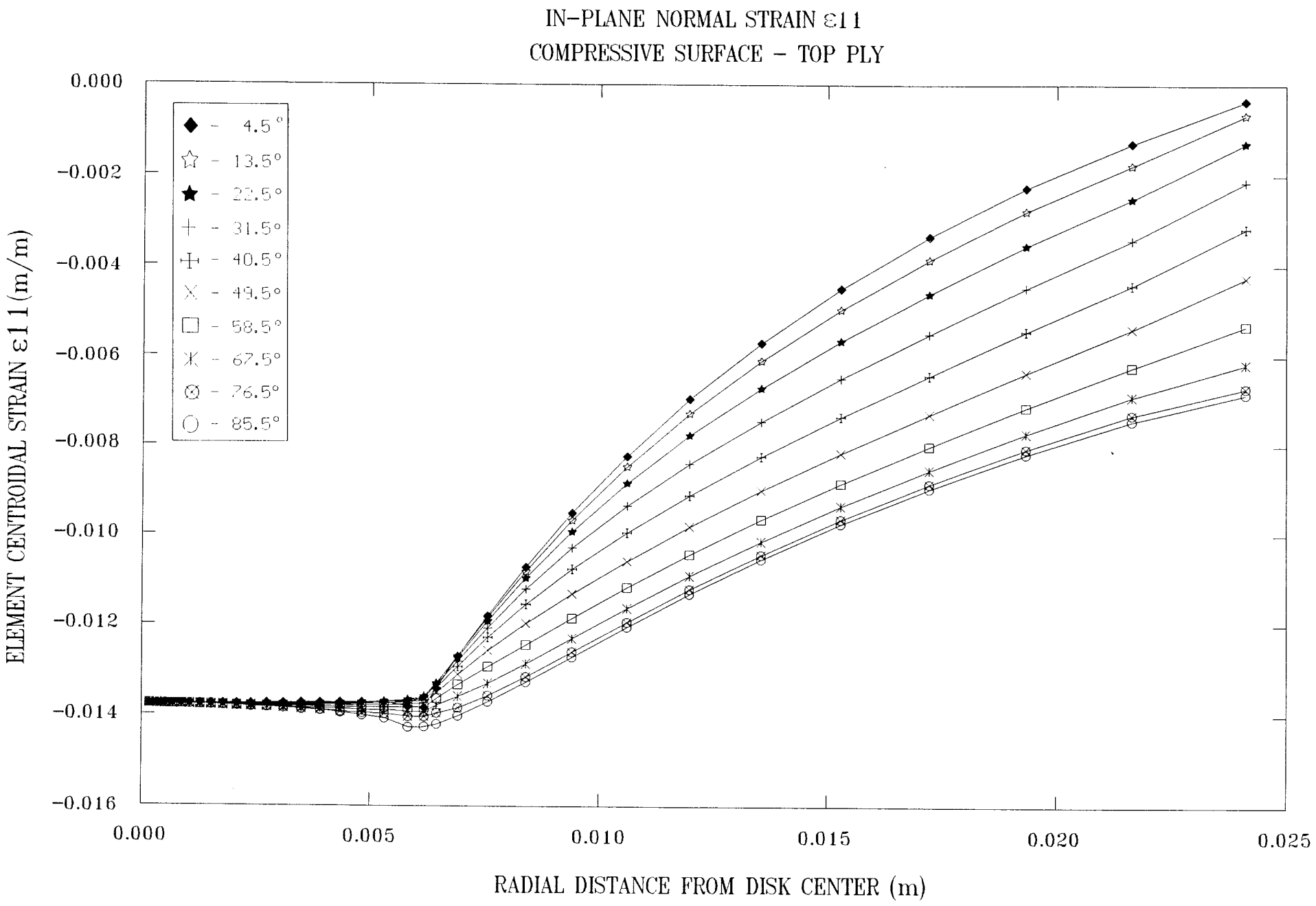

Fig.(6) ε_{11} PRINCIPAL STRAIN vs. DISTANCE - COMPRESSIVE SURFACE

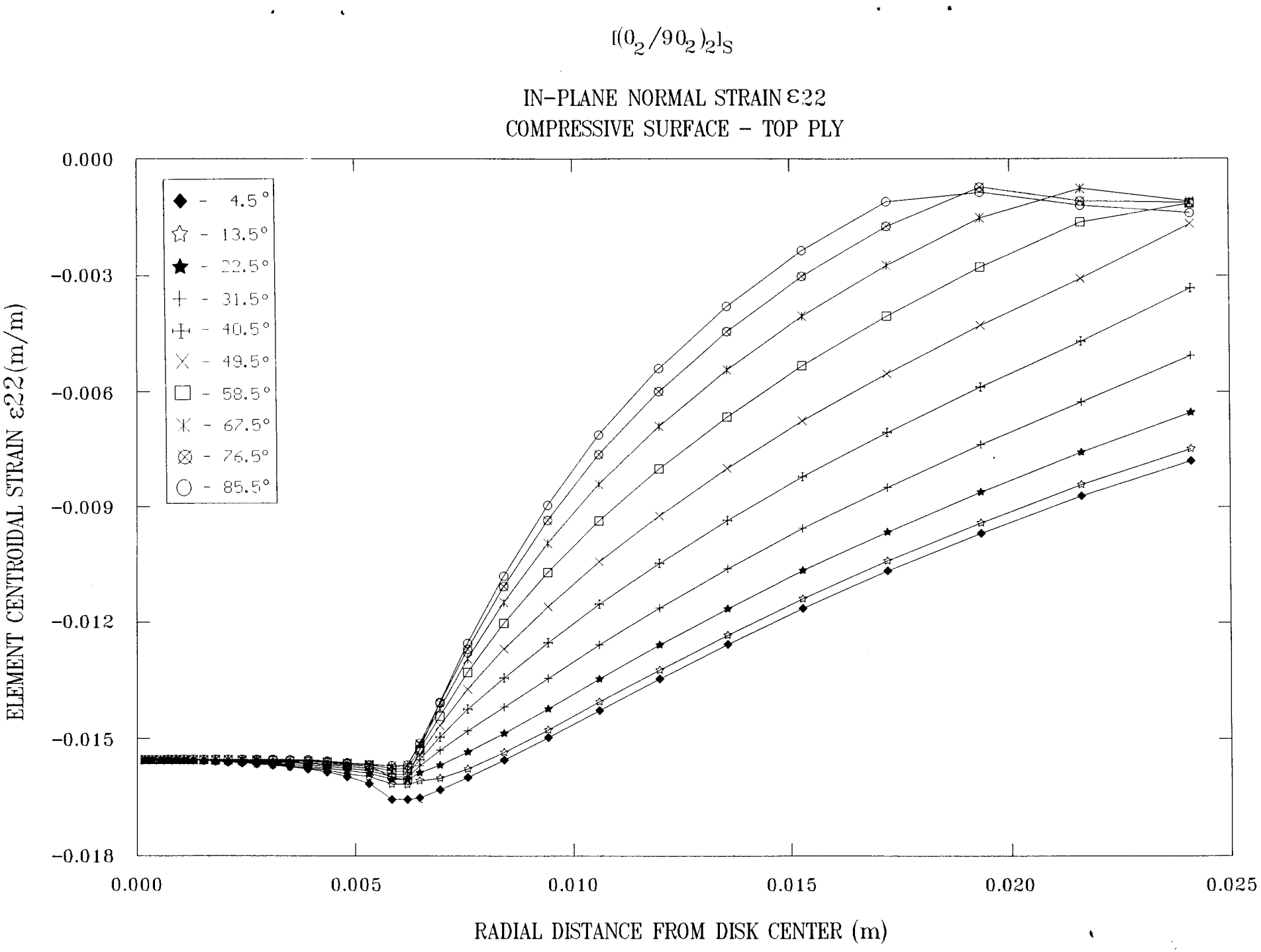

Fig.(7) ε_{22} PRINCIPAL STRAIN vs. DISTANCE - COMPRESSIVE SURFACE

$[(0_2/90_2)_2]_S$

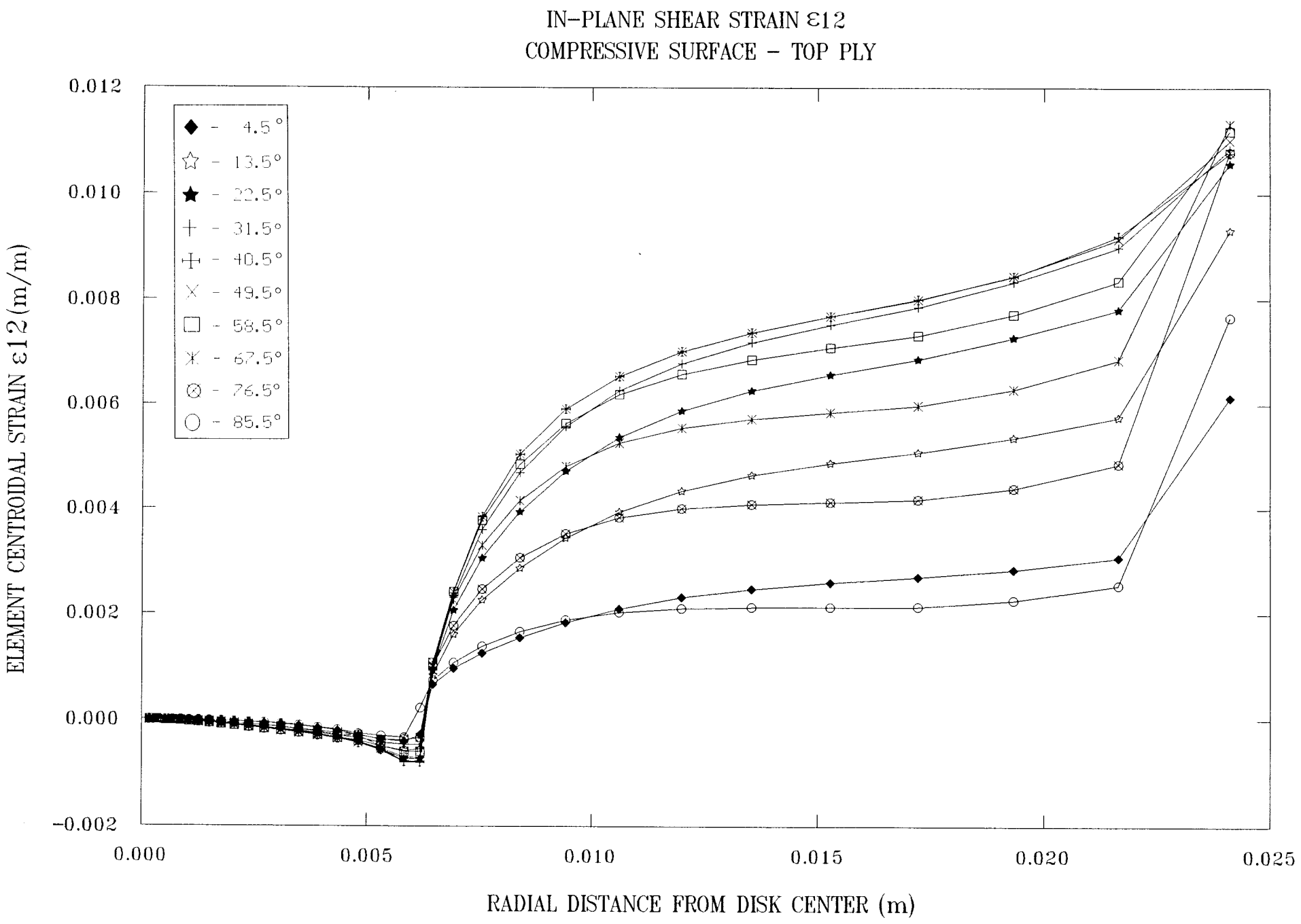

Fig. (8) ε_{12} PRINCIPAL STRAIN vs. DISTANCE - COMPRESSIVE SURFACE

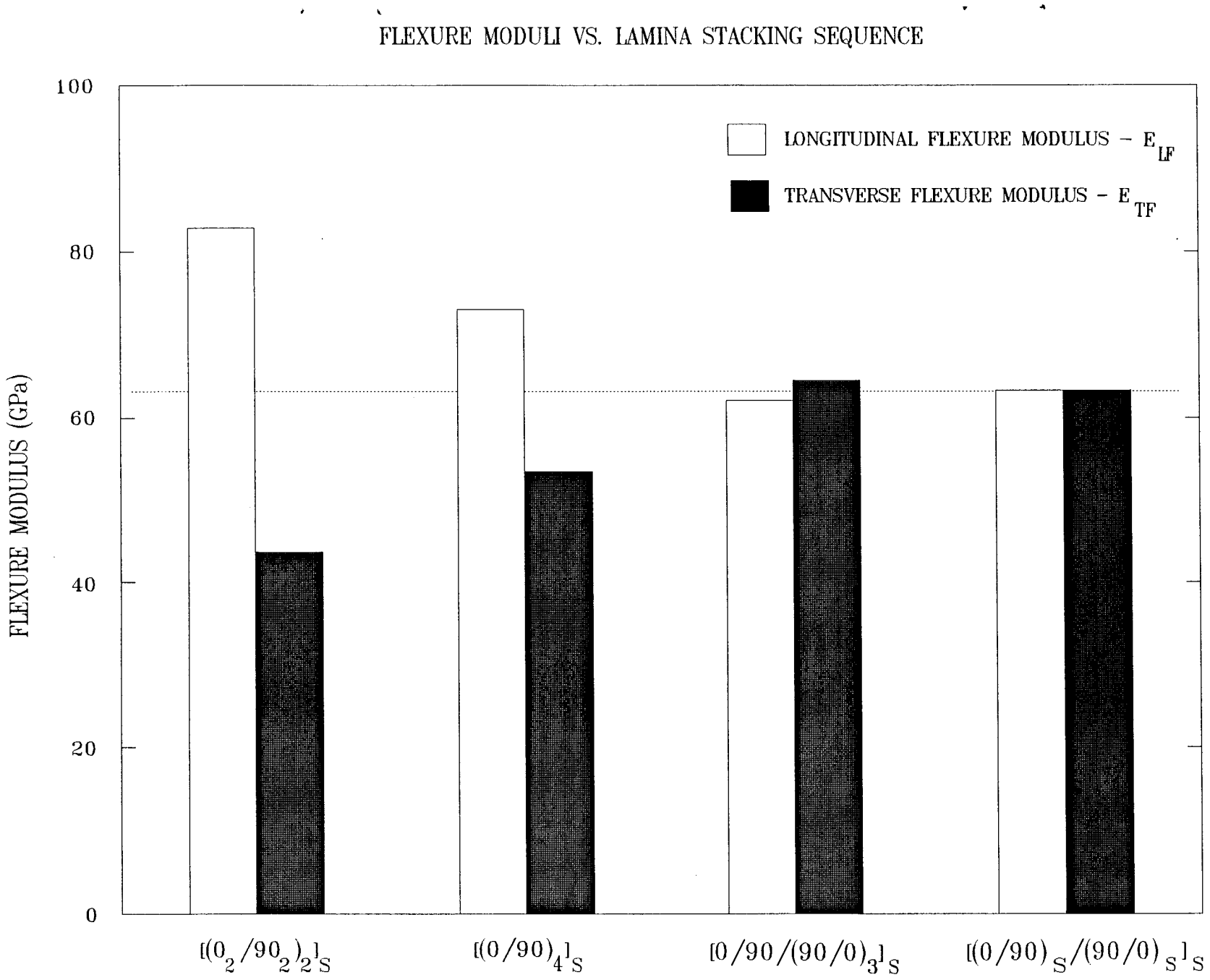

Fig.(9) FLEXURE MODULI vs. CROSS-PLY LAMINA STACKING SEQUENCE

(Z-AXIS PARALLEL TO DISK THICKNESS)

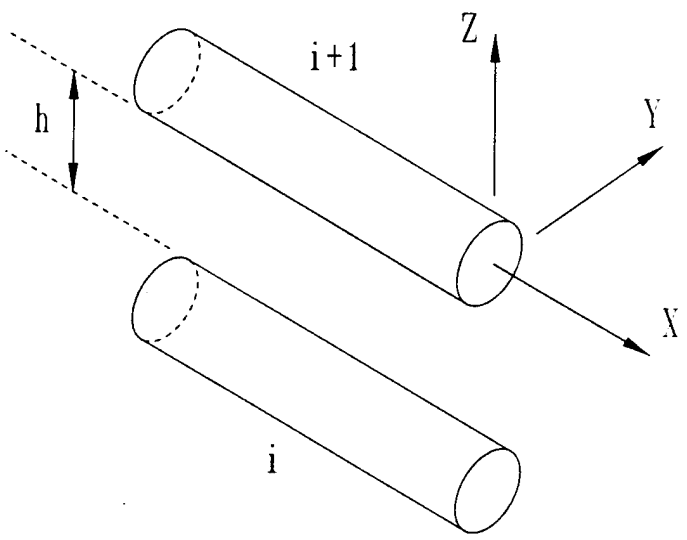

Fig.(10) EFFECT OF FIBER DIAMETER AND SPACING

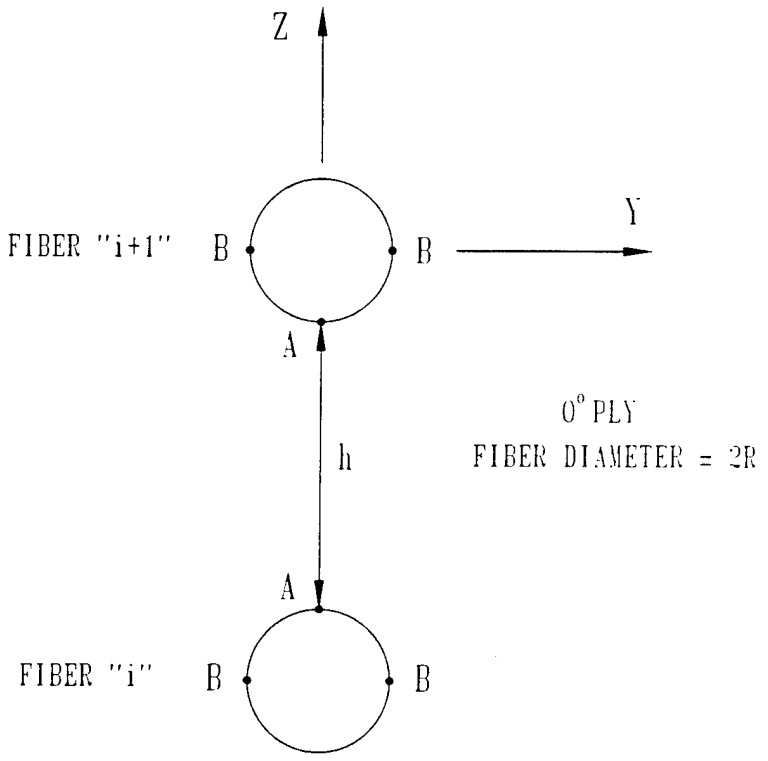

Fig.(11) LOCATIONS OF MAXIMUM/MINIMUM LOCAL SHEAR STRAINS

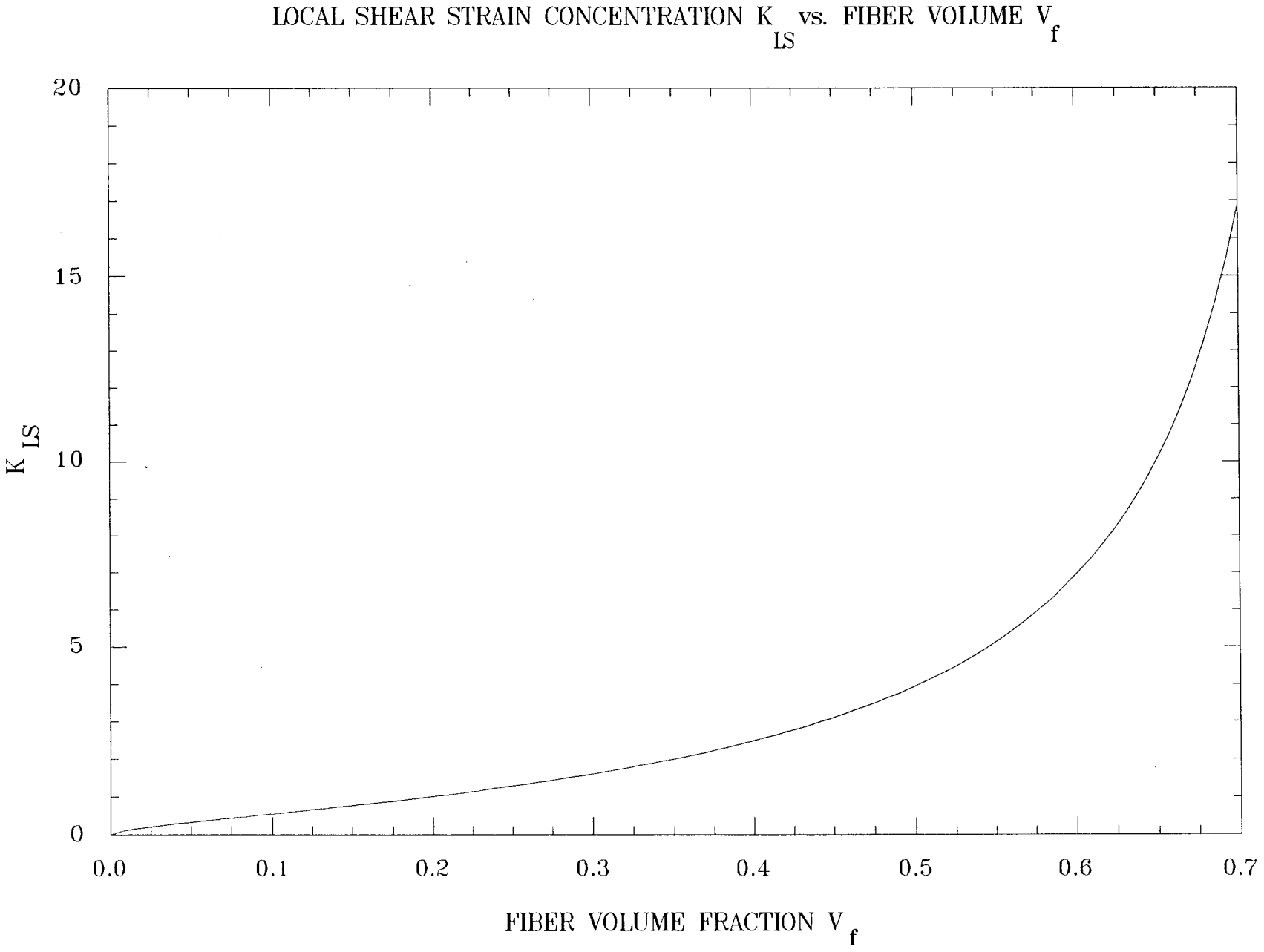

Fig.(12) LOCAL SHEAR STRAIN CONCENTRATION FACTOR K_{LS} vs. FIBER VOLUME FRACTION V_f

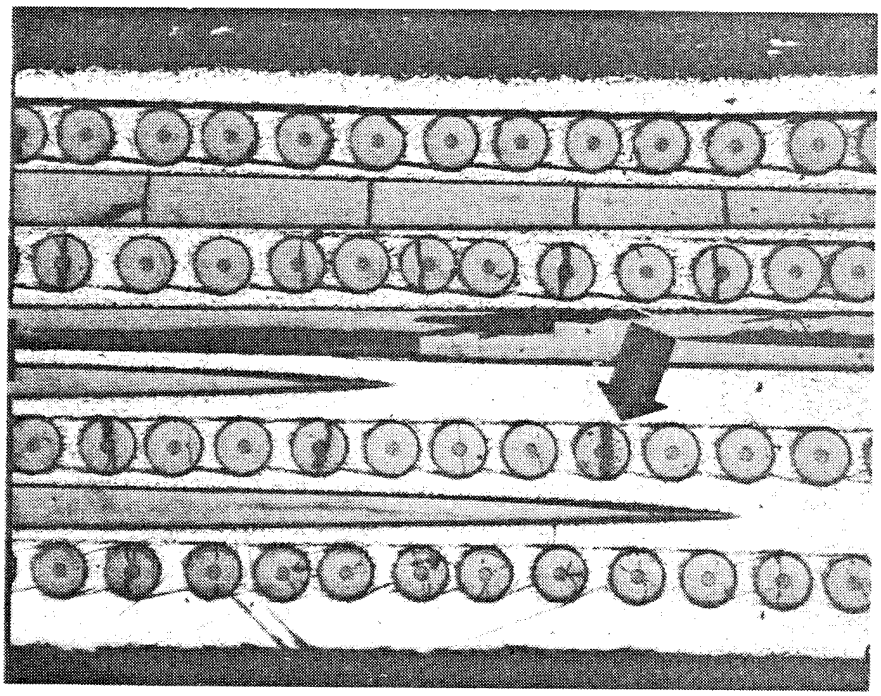

Fig.(13) INTERLAMINAR SHEAR CRACKS FORMED IN SILICON CARBIDE/ALUMINUM COMPOSITE DISK

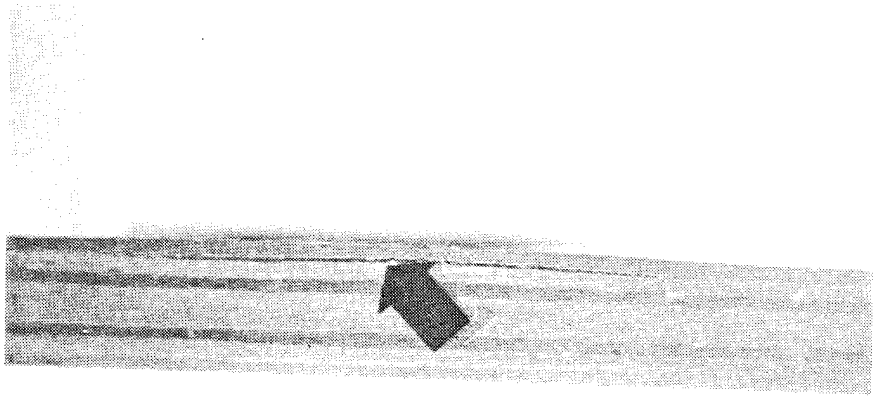

Fig.(14) INTERLAMINAR SHEAR CRACK FORMED IN GRAPHITE/EPOXY COMPOSITE DISK

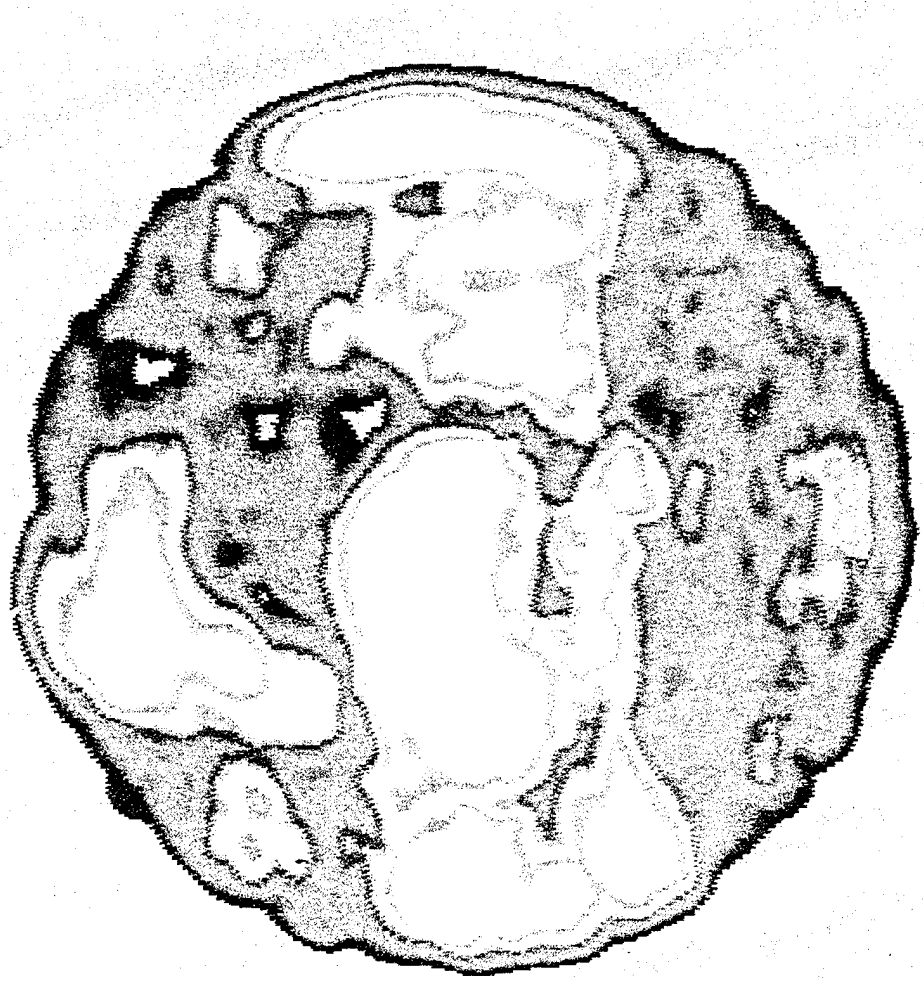

Fig.(15) C-SCAN OF GRAPHITE/EPOXY DISK WITH MULTIPLE CRACKS

DISTRIBUTION LIST

No. of Copies	To
1	Office of the Under Secretary of Defense for Research and Engineering, The Pentagon, Washington, DC 20301
	Director, U.S. Army Research Laboratory, 2800 Powder Mill Road, Adelphi, MD 20783-1197
1	ATTN: AMSRL-OP-SD-TP, Technical Publishing Branch
1	AMSRL-OP-SD-TA, Records Management
1	AMSRL-OP-SD-TL, Technical Library
	Commander, Defense Technical Information Center, Cameron Station, Building 5, 5010 Duke Street, Alexandria, VA 23304-6145
2	ATTN: DTIC-FDAC
1	MIA/CINDAS, Purdue University, 2595 Yeager Road, West Lafayette, IN 47905
	Commander, Army Research Office, P.O. Box 12211, Research Triangle Park, NC 27709-2211
1	ATTN: Information Processing Office
	Commander, U.S. Army Materiel Command, 5001 Eisenhower Avenue, Alexandria, VA 22333
1	ATTN: AMCSCI
1	AMCMI-IS-A
	Commander, U.S. Army Materiel Systems Analysis Activity, Aberdeen Proving Ground, MD 21005
1	ATTN: AMXSY-MP, H. Cohen
	Commander, U.S. Army Missile Command, Redstone Arsenal, AL 35809
1	ATTN: AMSMI-RD-CS-R/Doc
	Commander, U.S. Army - ARDEC, Information Research Center, Picatinny Arsenal, NJ 07806-5000
1	ATTN: AMSTA-AR-IMC, Bldg. 59
	Commander, U.S. Army Natick Research, Development and Engineering Center Natick, MA 01760-5010
1	ATTN: SATNC-MI, Technical Library
1	SATNC-AI
	Commander, U.S. Army Satellite Communications Agency, Fort Monmouth, NJ 07703
1	ATTN: Technical Document Center
	Commander, U.S. Army Tank-Automotive Command, Warren, MI 48397-5000
1	ATTN: AMSTA-ZSK
1	AMSTA-TSL, Technical Library
1	AMSTA-SF
	President, Airborne, Electronics and Special Warfare Board, Fort Bragg, NC 28307
1	ATTN: Library

No. of Copies	To
	Director, U.S. Army Research Laboratory, Weapons Technology, Aberdeen Proving Ground, MD 21005-5066
1	ATTN: AMSRL-WT
2	Technical Library
	Commander, Dugway Proving Ground, UT 84022
1	ATTN: Technical Library, Technical Information Division
	Commander, U.S. Army Research Laboratory, 2800 Powder Mill Road, Adelphi, MD 20783
1	ATTN: AMSRL-SS
	Director, Benet Weapons Laboratory, LCWSL, USA AMCCOM, Watervliet, NY 12189
1	ATTN: AMSMC-LCB-TL
1	AMSMC-LCB-R
1	AMSMC-LCB-RM
1	AMSMC-LCB-RP
	Commander, U.S. Army Foreign Science and Technology Center, 220 7th Street, N.E., Charlottesville, VA 22901-5396
3	ATTN: AIFRTC, Applied Technologies Branch, Gerald Schlesinger
	Commander, U.S. Army Aeromedical Research Unit, P.O. Box 577, Fort Rucker, AL 36360
1	ATTN: Technical Library
	U.S. Army Aviation Training Library, Fort Rucker, AL 36360
1	ATTN: Building 5906-5907
	Commander, U.S. Army Agency for Aviation Safety, Fort Rucker, AL 3636
1	ATTN: Technical Library
	Commander, Clarke Engineer School Library, 3202 Nebraska Ave., N., Fort Leonard Wood, MO 65473-5000
1	ATTN: Library
	Commander, U.S. Army Engineer Waterways Experiment Station, P.O. Box 631, Vicksburg, MS 39180
1	ATTN: Research Center Library
	Commandant, U.S. Army Quartermaster School, Fort Lee, VA 23801
1	ATTN: Quartermaster School Library
	Naval Research Laboratory, Washington, DC 20375
1	ATTN: Code 6384
	Chief of Naval Research, Arlington, VA 22217
1	ATTN: Code 471
	Commander, U.S. Air Force Wright Research and Development Center, Wright-Patterson Air Force Base, OH 45433-6523
1	ATTN: WRDC/MLLP, M. Forney, Jr.
1	WRDC/MLBC, Mr. Stanley Schulman

No. of Copies	To
	U.S. Department of Commerce, National Institute of Standards and Technology, Gaithersburg, MD 20899
1	ATTN: Stephen M. Hsu, Chief, Ceramics Division, Institute for Materials Science and Engineering
1	Committee on Marine Structures, Marine Board, National Research Council, 2101 Constitution Avenue, N.W., Washington, DC 20418
1	Materials Sciences Corporation, Suite 250, 500 Office Center Drive, Fort Washington, PA 19034
1	Charles Stark Draper Laboratory, 555 Technology Square, Cambridge, MA 02139
	General Dynamics, Convair Aerospace Division, P.O. Box 748, Fort Worth, TX 76101
1	ATTN: Mfg. Engineering Technical Library
	Plastics Technical Evaluation Center, PLASTEC, ARDEC, Bldg. 355N, Picatinny Arsenal, NJ 07806-5000
1	ATTN: Harry Pebly
1	Department of the Army, Aerostructures Directorate, MS-266, U.S. Army Aviation R&T Activity - AVSCOM, Langley Research Center, Hampton, VA 23665-5225
1	NASA - Langley Research Center, Hampton, VA 23665-5255
	U.S. Army Vehicle Propulsion Directorate, NASA Lewis Research Center, 2100 Brookpark Road, Cleveland, OH 44135-3191
1	ATTN: AMSRL-VP
	Director, Defense Intelligence Agency, Washington, DC 20340-6053
1	ATTN: ODT-5A, Mr. Frank Jaeger
	U.S. Army Communications and Electronics Command, Fort Monmouth, NJ 07703
1	ATTN: Technical Library
	U.S. Army Research Laboratory, Electronic Power Sources Directorate, Fort Monmouth, NJ 07703
1	ATTN: Technical Library
	Director, U.S. Army Research Laboratory, Watertown, MA 02172-0001
2	ATTN: AMSRL-OP-WT-IS, Technical Library
15	Authors